Bioactive Materials 7 (2022) 112–125

Contents lists available at ScienceDirect

Bioactive Materials

journal homepage: www.sciencedirect.com/journal/bioactive-materials

Aggregation-induced emission luminogens for highly effective microwave dynamic therapy

Nil Kanatha Pandey [a], Wei Xiong [b], Lingyun Wang [a,b,**], Wei Chen [a,*], Brian Bui [a], Jian Yang [c], Eric Amador [a], Mingli Chen [d], Christina Xing [a], Aseem Atul Athavale [e], Yaowu Hao [e], Wirya Feizi [f], Lloyd Lumata [f]

[a] Department of Physics, The University of Texas at Arlington, Arlington, TX 76019, USA
[b] Key Laboratory of Functional Molecular Engineering of Guangdong Province, School of Chemistry and Chemical Engineering, South China University of Technology, Guangzhou, 510640, China
[c] Department of Biomedical Engineering, The Pennsylvania State University, University Park, PA, 16802, USA
[d] Department of Chemistry, College of Sciences, Northeastern University, Box 332, Shenyang 110819, China
[e] Department of Materials Science and Engineering, The University of Texas at Arlington, Arlington, TX 76019, USA
[f] Department of Physics, The University of Texas at Dallas, 800 West Campbell Road, Richardson, TX 75080, USA

ARTICLE INFO

Keywords:
AIEgens
Microwaves
Photodynamic therapy
Reactive oxygen species
Microwave ablation
Cancer treatment
Singlet oxygen

ABSTRACT

Aggregation-induced emission luminogens (AIEgens) exhibit efficient cytotoxic reactive oxygen species (ROS) generation capability and unique light-up features in the aggregated state, which have been well explored in image-guided photodynamic therapy (PDT). However, the limited penetration depth of light in tissue severely hinders AIEgens as a candidate for primary or adjunctive therapy for clinical applications. Coincidentally, microwaves (MWs) show a distinct advantage for deeper penetration depth in tissues than light. Herein, for the first time, we report AIEgen-mediated microwave dynamic therapy (MWDT) for cancer treatment. We found that two AIEgens (**TPEPy-I** and **TPEPy-PF6**) served as a new type of microwave (MW) sensitizers to produce ROS, including singlet oxygen ($^1O_2$), resulting in efficient destructions of cancer cells. The results of 3-(4,5-dimethylthiazol-2-yl)-2,5-diphenyltetrazolium bromide (MTT) and live/dead assays reveal that the two AIEgens when activated by MW irradiation can effectively kill cancer cells with average IC-50 values of 2.73 and 3.22 μM, respectively. Overall, the ability of the two AIEgens to be activated by MW not only overcomes the limitations of conventional PDT, but also helps to improve existing MW ablation therapy by reducing the MW dose required to achieve the same therapeutic outcome, thus reducing the occurrence of side-effects of MW radiation.

1. Introduction

Photodynamic therapy (PDT), a promising cancer treatment modality with minimal invasiveness, negligible drug resistance and low side effects, employs a photosensitizer (PS) that can be excited by light of suitable wavelength to form ROS, which can induce apoptosis and/or necrosis in treated cells. Also, PDT can be used either on its own or in combination with other therapeutic modalities, such as surgery, chemotherapy, radiotherapy, or immunotherapy [1–3]. Even though PDT has great potential for clinical use, conventional PSs generally suffer from aggregation-caused fluorescence quenching and a significant reduction in ROS production in aqueous media [4–7]. Fortunately, aggregation-induced emission luminogens (AIEgens) offer a potential opportunity to overcome this limitation. AIEgens refer to special types of molecules that are barely emissive in the molecularly dissolved state but emit intense fluorescence in the aggregation state due to the restriction of intramolecular motion [4]. Intriguingly, several AIEgens show efficient photosensitizing ability and unique light-up features in the aggregated state, which are beneficial to develop image-guided PDT for cancer treatment [5–8]. However, the poor penetration depth of light still hinders AIE PSs as primary or adjunctive therapy for clinical application. Furthermore, due to the oxygen-dependent nature of PDT

Peer review under responsibility of KeAi Communications Co., Ltd.
* Corresponding author.
** Corresponding author. School of Chemistry and Chemical Engineering, South China University of Technology, Guangzhou, China.
E-mail addresses: lingyun@scut.edu.cn (L. Wang), weichen@uta.edu (W. Chen).

https://doi.org/10.1016/j.bioactmat.2021.05.031
Received 3 February 2021; Received in revised form 5 May 2021; Accepted 20 May 2021
Available online 3 June 2021

[9], it is noted that both types of PSs (conventional and AIE) are less effective in treating hypoxic tumors, further limiting their practicality in clinical settings.

As an alternative modality of tumor destruction, thermal ablation has been extensively explored in the clinical setting. It is considered as one of the most effective treatments in combined oncotherapy as it leads to improved tumor sensitization to PDT, chemotherapy, immunotherapy, or radiotherapy [10–14] because the blood flow to the tumor is enhanced through heating. When the tissues are heated, the blood vessels dilate, which increases blood flow. As hemoglobin in blood contains oxygen, tissue heating boosts the amount of oxygen, thereby enhancing the efficacy of the treatments [10,11]. Compared with other thermal therapies, MW technology has many advantages, such as maneuverability, faster ablation time, deeper penetration in tissues, larger tumor ablation volumes, less procedural pain, consistently higher intratumoral temperature, and negligible side effects [10,15–17]. Notably, MWs are readily capable of propagating through many types of tissues and nonmetallic materials, including charred or desiccated tissues created during the process of ablation [15]. Despite these advantages, the lack of selectivity of MWs on tumors may cause severe damage to the surrounding normal tissues during the course of treatment [2]. Consequently, further study and continued development of a more robust system are still needed to minimize nonspecific heating of healthy tissues.

Recently, microwave dynamic therapy (MWDT) has attracted broad attention, in which MW sensitizers can produce ROS under MW irradiation to destroy tumor cells. Various MW-responsive agents such as copper-cysteamine (Cu-Cy) nanoparticles [18,19], g-C_3N_4 quantum dots [20], TiO_2 nanoparticles [21], Fe-metal organic framework nanoparticles [22], liquid metal supernanoparticles [23], Cu_2ZnSnS_4 nanocrystals [24], Mn-doped zirconium metal-organic framework nanocubes [25], and gold nanoparticles [26] have been reported to produce ROS upon MW radiation. All of these sensitizers are sensitive to MWs and attractive for applications with MWs; however, the toxic nature of some of these metal ions and/or high concentration of sensitizers could result in severe side effects. Therefore, the exploration of more efficient sensitizers that are capable of avoiding the above limitations is of great importance to improve the therapeutic effect of MWDT.

In our previous work, pyridinium-substituted tetraphenylethylene salt-based AIEgens (**TPEPy-I** and **TPEPy-PF6**, Scheme 1) exhibited PDT effect for cancer cell destruction and bacterial inactivation under white light irradiation [27]. However, to the best of our knowledge, there is no report on AIEgen-mediated ROS production under MW irradiation. The reason may be that MW has an energy of only 10^{-3} eV, which is too low to cleave chemical bonds and induce ROS generation [23,28]. Considering these two AIEgens comprise of a TPE segment (donor), a thiophene vinyl fragment (π bridge), and a cationic pyridinium moiety (acceptor) with a strong charge-transfer feature and effective ISC channels with a small ΔE_{S_T} ($S_1 \rightarrow T_3$: -0.22 eV), it is possible for them to be activated by MW irradiation to generate ROS.

In this contribution, for the first time, the two AIEgens (**TPEPy-I** and **TPEPy-PF6**) are reported as MW sensitizers with efficient ROS generation and cancer cell killing capabilities under MW irradiation. Overall, this work opens the door to treat tumors using AIEgens under MW irradiation and makes conventional PDT possible for deep cancer treatment, even in the context of hypoxic environments.

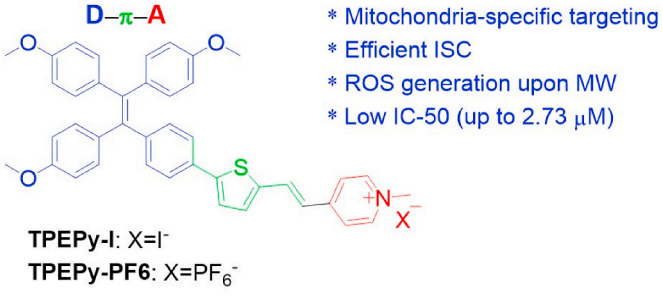

Scheme 1. The chemical structures of two MW sensitizers (**TPEPy-I** and **TPEPy-PF6**).

2. Materials and methods

2.1. Materials

p-Nitrosodimethylaniline (RNO), imidazole, 1,4-benzoquinone (BQ), sodium azide (NaN_3), 2′,7′-dichlorodihydrofluorescein diacetate (DCFH-DA), 9,10-anthracenediyl-bis(methylene)dimalonic acid (ABDA), 2,2,6,6-tetramethylpiperidine (TEMP), and 1,4-diazabicyclo[2.2.2]octane (DABCO) were obtained from Sigma-Aldrich, USA. 3-(4,5-dimethylthiazol-2-yl)-2,5-diphenyltetrazolium bromide (MTT) was purchased from Thermo Fisher Scientific, USA. All the chemicals were used as received without further purification.

2.2. UV–vis absorption and fluorescence spectroscopy

TPEPy-I and **TPEPy-PF6** (stock solution in DMF) were dispersed in DI water, and the UV–vis optical absorption and photoluminescence spectra were measured by using a Shimadzu UV–Vis spectrophotometer (UV-2450) and a Shimadzu spectrofluorophotometer (RF-5301PC), respectively.

2.3. Scanning electron microscopy (SEM) and fluorescence microscopy imaging

The SEM images were taken by using a Hitachi S-4800 FE-SEM. For SEM measurements, samples were dropped on the surface of the silicon substrate and then dried to obtain dried samples. In order to obtain fluorescence microscopy images, **TPEPy-I** or **TPEPy-PF6** was dropped into an imaging plate and then observed using an OLYMPUS IX71 fluorescence microscope.

2.4. ROS detection in cell-free system using RNO bleaching method

We employed the RNO bleaching method [29] to probe the extracellular ROS production upon MW excitation. The intensity of RNO absorption was recorded spectrophotometrically at different time points of MW exposure (2450 MHz). The MW was delivered in a dark condition through a radiator probe employing a microwave therapy apparatus (WB-3100AI, BXING, China). Briefly, 0.45 mg of RNO and 32.68 mg of imidazole were dissolved separately into 30 mL of DI water, which were subsequently air saturated by air bubbling for 15 min. Afterward, the RNO-imidazole solution (final volume 3 mL) was prepared under the dark condition in a cuvette (10 mm path length) by mixing 1 mL of RNO, 1 mL of imidazole, and 1 mL of the testing sample. Meanwhile, as a reference, the control experiment was carried out following the same procedure, except the testing sample was replaced by DI water to see the effect of MW irradiation on RNO's absorption.

2.5. Singlet oxygen ($^1O_2$) detection in aqueous solution using ABDA probe and electron spin resonance (ESR) spectroscopy

In order to further support the $^1O_2$ production under MW activation, $^1O_2$ produced by the **TPEPy-I** and **TPEPy-PF6** nanoaggregates were also measured by employing the commercially available probe ABDA as a $^1O_2$ indicator [30]. Briefly, the stock solution of ABDA (1.5 mM) was made in DMF. The working solution (final volume 3 mL) was prepared in DI water by taking 30 μM of ABDA and 15 μM of **TPEPy-I** or **TPEPy-PF6** in a 10 mm path length cuvette under dark condition. The solution was then exposed to MW (2450 MHz) in the dark for various periods, and the absorbance of ABDA was monitored at 379 nm by the

spectrophotometer. The control experiment was performed by taking DI water alone instead of the testing sample under the same conditions to compare the effect of MW on the absorbance of ABDA.

The ESR measurements were conducted at the Nanotech Institute at the University of Texas at Dallas by using a Bruker EMX X-band ESR spectrometer (Bruker Biospin, Billerica, MA). A small aliquot of each sample was placed in 0.5-mm ID heparinized hematocrit capillary tubes, which were subsequently placed in 4-mm thin wall quartz ESR tubes (Wilmad Lab-Glass, Vineland, NJ). Field-swept continuous wave ESR spectra were recorded at room temperature.

2.6. Extracellular ROS detection using DCFH-DA probe

The ROS produced by the **TPEPy-I** and **TPEPy-PF6** nanoaggregates in aqueous solution upon MW excitation was further investigated by the photoluminescence (PL) method using DCFH-DA as a ROS probing agent [8,23]. The stock solution of DCFH-DA (1.8 mM) was made in DMF. After that, the working solution (final volume 3 mL) containing DCFH-DA (30 μM) and **TPEPy-I** or **TPEPy-PF6** (10 μM) was prepared in a cuvette (10 mm path length) under the dark condition. The solution was then exposed to MW (2450 MHz) in the dark for various periods, and the PL intensity was subsequently recorded at 523 nm by the spectrofluorophotometer with the excitation wavelength of 505 nm. The control experiment was performed by taking DI water instead of **TPEPy-I** and **TPEPy-PF6** under the same conditions.

2.7. Detection of intracellular ROS production

We studied the intracellular generation of ROS using DCFH-DA as a fluorescence detection probe [31]. 1×10^5 HeLa cells per imaging plate were seeded into nine different imaging plates and incubated in a humidified cell incubator containing 5% CO_2 at 37 °C for 24 h. Afterward, the cells were incubated with or without **TPEPy-I** and **TPEPy-PF6** (5 μM) for 4 h in the fresh culture medium (3 mL). Cells were then washed with PBS twice and incubated with 20 μM of DCFH-DA in DMEM (500 μL) for another 45 min at 37 °C in the dark. The cells were subsequently washed three times with PBS in order to remove the unloaded probe. The indicated cells were then exposed to 10 W (2450 MHz) of MW irradiation (inserting the MW probe into the medium without touching the cells) in the dark condition for 1 or 1.5 min after adding 3 mL of DMEM. Finally, the cells were resuspended in PBS (500 μL) and immediately observed using the OLYMPUS IX71 fluorescence microscope under the same instrumental conditions.

2.8. Microwave dynamic therapy (MWDT) study using MTT assay

The cytotoxicity of **TPEPy-I** and **TPEPy-PF6** nanoaggregates under MW irradiation was investigated using MTT assay. HeLa cells were seeded in 24-well plates at a density of 2×10^4 cells/well. After allowing to attach and grow for 24 h, the old medium was removed from each well, and 2.4 mL of fresh culture medium (DMF-culture medium with 99.92% culture medium content) containing various concentrations of **TPEPy-I** or **TPEPy-PF6** (0–10 μM) were added to each well. After 4 h of additional incubation, the cells were treated with or without 10 W of MW radiation (2450 MHz) in the dark condition for 1.5 min (inserting the probe of MW into the culture medium without touching the surface of the plate) and further incubated for 20 h. The old medium was then removed, and 400 μL of fresh culture medium containing 40 μL of MTT solution (5 mg/mL MTT reagent in PBS) was added to each well and incubated for another 4 h in the dark. Then, the formazan product was solubilized by adding DMSO, and the absorption of the formazan crystal was recorded at 540 nm using a microplate reader (Multiskan FC). Finally, cell viability was determined using the following equation:

$$\text{Cell viability} = \frac{\text{The absorbance of the treated group}}{\text{The absorbance of the untreated group}} \times 100\%$$

2.9. Investigation of MWDT effect using live/dead assay

We further explored the cell viability under MW irradiation by using a live/dead assay. HeLa cells were cultured at a density of 1×10^5 cells/well and then incubated at 37 °C in a humidified 5% v/v CO_2 atmosphere in a cell incubator for 24 h. Following the incubation, the old medium was removed, and 3 mL of fresh medium (DMF-culture medium with 99.92% culture medium content) with or without 10 μM of **TPEPy-I** and **TPEPy-PF6** was then added to each well. There were nine groups: control, **TPEPy-I**, **TPEPy-PF6**, 1.5 min MW, 2 min MW, **TPEPy-I** + 1.5 min MW, **TPEPy-I** + 2 min MW, **TPEPy-PF6** + 1.5 min MW, and **TPEPy-PF6** + 2 min MW. After incubating for 4 h, the MW, **TPEPy-I** + MW, and **TPEPy-PF6** + MW groups were irradiated with 1.5 or 2 min of MW (10 W; 2450 MHz) through the radiator probe (inserting the probe into the medium without touching the plate surface) in the dark condition. Afterward, the cells were incubated in the incubator for 20 h. On the day of the experiment, the old medium was replaced with 500 μL of fresh medium containing a mixture of calcein-AM and propidium iodide (PI) and incubated for another 45 min at 37 °C under the dark condition. Finally, the stained cells were visualized by the OLYMPUS IX71 fluorescence microscope.

2.10. Bright-field imaging

In order to observe the changes in the morphology of the cells after MW treatments, bright-field images of the HeLa cells were collected with the help of the OLYMPUS IX71 fluorescence microscope.

2.11. Statistical analysis

The data represented as mean ± standard deviation was performed at least three times. One-way analysis of variance (ANOVA) followed by the Tukey test was employed to determine the statistical significance between the control and the experimental groups. A p-value < 0.05 was considered statistically significant.

3. Results and discussion

3.1. Synthesis and characterization of TPEPy-I and TPEPy-PF6

The synthesis and detailed characterizations of the two AIEgens **TPEPy-I** and **TPEPy-PF6** (Scheme 1) have been described in our recent publication [27]. Fig. 1a illustrates the absorption spectra of the **TPEPy-I** and **TPEPy-PF6** nanoaggregates in DMF-water mixture (99.75% water), with the absorption maxima at about 440 and 450 nm, respectively. Fig. 1b depicts the PLE and PL spectra of the **TPEPy-I** and **TPEPy-PF6** nanoaggregates in DMF-water mixture (99.75% water), with the emission maxima at about 652 and 663 nm, respectively, when excited at 467 nm. Moreover, their PL spectra were found to be almost the same even after 4 months of storage (Fig. S1), demonstrating their good stability. Dynamic light scattering (DLS) measurements revealed that the mean hydrodynamic diameters of the nanoaggregates that formed in the DMF-water mixture (99.67% water) were (119 ± 32) and (152 ± 48) nm for **TPEPy-I** and **TPEPy-PF6** nanoaggregates (Fig. 1c and d), respectively.

3.2. Scanning electron microscopy (SEM) and fluorescence microscopy images

We used SEM to investigate the morphology and self-assembly behaviors of both AIEgens. Fig. 2a–f shows that both AIEgens self-assembled into nano/micro-architectures when no water was used. We further carried out SEM measurements when water contents on both AIEgens were 90% and 99.67%. As depicted in Fig. 2g-o, molecules self-assembled into micro-/nanostructures after the evaporation of water. As

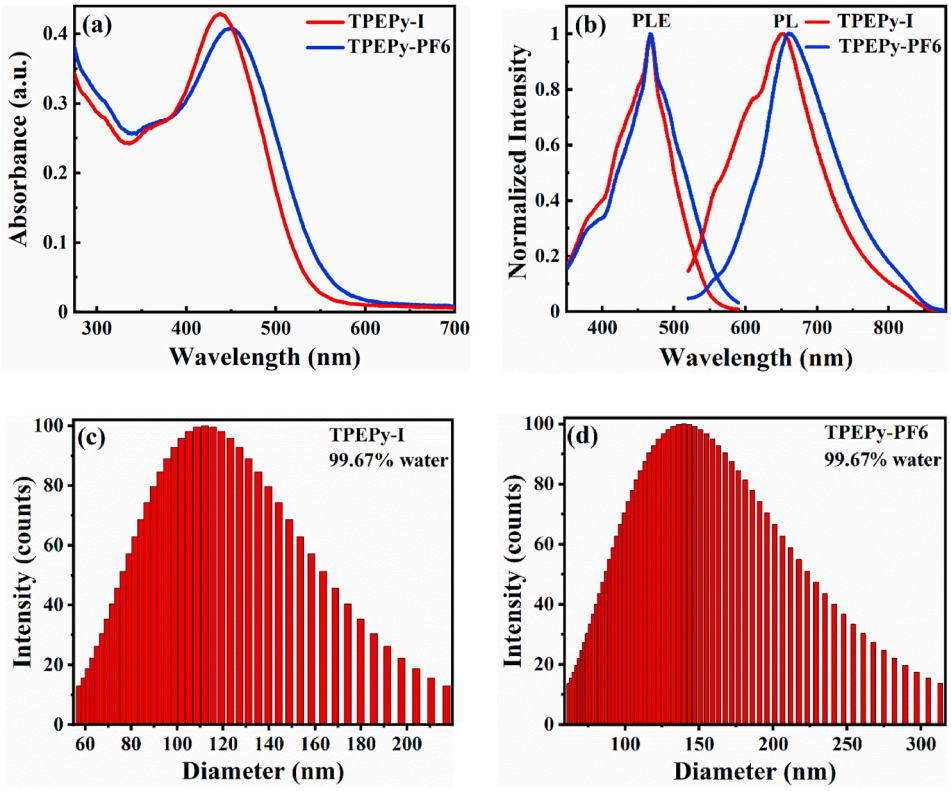

Fig. 1. (a) UV–vis absorption spectra of **TPEPy-I** and **TPEPy-PF6** nanoaggregates in the DMF-water mixture with 99.75% water content. (b) Normalized photoluminescence excitation (PLE) spectra at 467 nm (left) and PL emission spectra at 652 and 663 nm (right) of the **TPEPy-I** and **TPEPy-PF6** nanoaggregates, respectively, in DMF-water mixture with 99.75% water content. Emission wavelengths of **TPEPy-I** and **TPEPy-PF6** nanoaggregates were 652 and 663 nm, respectively. The excitation wavelength was 467 nm for both cases. (c and d) Particle size distribution of (c) **TPEPy-I** and (d) **TPEPy-PF6** nanoaggregates in DMF-water mixture with 99.67% water content measured by DLS.

solvent needs to be evaporated before performing SEM measurements, only slight difference was observed under different conditions. Since the properties of these AIEgens strongly depend upon water content and all water contents were evaporated before SEM observations, SEM results showed a broader range of sizes than that of DLS measurements. The results of SEM observations suggest that both AIEgens were assembled into different shapes, as it is not easy for AIEgens to self-assemble into well-defined structures due to the nonpolar topology of AIEgens [32]. The aggregation behavior of AIEgens, in essence, is a self-assembly process primarily driven by the solvophobic effect of the molecules [33]. Fig. S2 shows one of the morphologies of **TPEPy-I** nanoaggregates when molecules of **TPEPy-I** assembled into nanoaggregates.

Additionally, the fluorescence microscopy images clearly showed bright red luminescence in the solid-state (powder samples), and the intensity of red luminescence increased with the size of aggregates (Fig. S3), further indicating that these are AIE-active molecules.

3.3. ROS detection in aqueous solution using RNO bleaching assay

ROS produced by the two AIEgens under MW irradiation was investigated by the RNO bleaching (RNO-imidazole) method [29]. In this spectrophotometric method, the reaction of $^1O_2$ with imidazole yields a transannular peroxide, which then reacts with RNO and causes bleaching of RNO that can be measured at 440 nm [29]. Firstly, we compared the ROS production ability of **TPEPy-I** and **TPEPy-PF6** nanoaggregates (10 μM) under 10 W of MW exposure by monitoring the absorbance of RNO at 440 nm as a function of MW exposure time. As presented in Fig. 3a, the absorbance of RNO was markedly reduced as compared to DI water alone, indicating that the two nanoaggregates could produce ROS when excited by MW. To ascertain that the decrease in the absorption of RNO was due to ROS generation, time-dependent UV–vis absorption spectra of both nanoaggregates (without MW activation) were recorded. As depicted in Fig. S4, the absorption intensity of both nanoaggregates at 440 nm did not vary noticeably over time, showing that the decrease in RNO absorbance was actually ascribed to the generated ROS from the two nanoaggregates.

It is interesting that **TPEPy-I** induced more ROS, which could be attributed to the positive effect of iodide anions as described in our recent work [34]. An alternative explanation might be due to the smaller size of **TPEPy-I** nanoaggregates (Fig. 1c and d) as smaller particles have larger surface areas, which are helpful to regulate the number of reactive sites on the particles' surface [35]. However, the exact cause of the difference in ROS generation capacity of the two samples is currently not known.

As discussed above, the ROS production performance of **TPEPy-I** nanoaggregates is better than that of **TPEPy-PF6**, motivating us to carry out further experiments on **TPEPy-I** nanoaggregates. Fig. 3b shows the comparison of ROS induced by **TPEPy-I** nanoaggregates (10 μM) at 2 and 10 W of MW irradiation. The result indicates that a higher MW dose produces more ROS. Furthermore, ROS production is also dependent on the concentration of the sample (Fig. 3c). Interestingly, 5 μM of **TPEPy-I** nanoaggregates under 10 W of MW produced the approximately same amount of ROS as that of 10 μM under 2 W of MW (Fig. 3c). Taken together, irradiation time, MW dose, and sample concentration proved to be key factors influencing ROS generation.

To test whether the ROS detected from the RNO bleaching assay was $^1O_2$, we added sodium azide (NaN_3), a physical quencher of $^1O_2$ [36], to **TPEPy-I** nanoaggregates under the same conditions. As displayed in Fig. 3d, the bleaching of RNO was noticeably reduced in the presence of NaN_3 (40 mM) because of the capture of $^1O_2$ by NaN_3, supporting that $^1O_2$ was the main component of the generated ROS.

We all know that $^1O_2$ is usually generated by the energy transfer from the excited state of PSs to molecular oxygen ($^3O_2$). However, some groups revealed that $^1O_2$ may be produced through the oxidation of superoxide radical ($\bullet O_2^-$) under appropriate conditions [37–41]. To verify this hypothesis, we added 1,4-benzoquinone (BQ), a well-known quencher of $\bullet O_2^-$ [42,43], into the solution of **TPEPy-I** nanoaggregates. Interestingly, the introduction of BQ (340 μM) into the solution of **TPEPy-I** nanoaggregates inhibited bleaching of RNO remarkably (Fig. 3d), indicating $\bullet O_2^-$ was simultaneously produced in the reaction

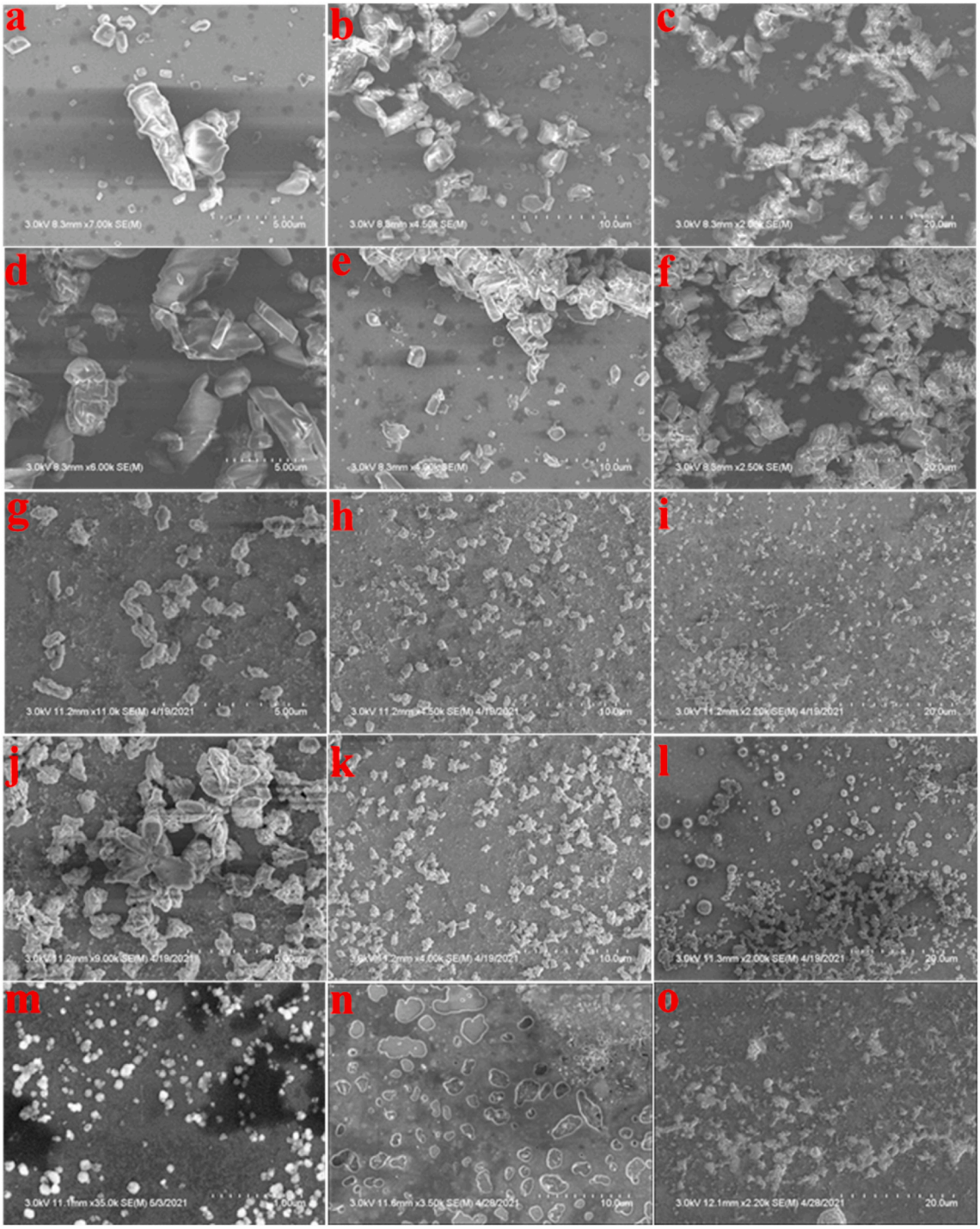

Fig. 2. Representative SEM images of (a–c) **TPEPy-I** with no water (powder sample), (d–f) **TPEPy-PF6** with no water (powder sample), (g–i) **TPEPy-I** with 90% water content, (j–l) **TPEPy-PF6** with 90% water content, (m–n) **TPEPy-I** with 99.67% water content, and (o) **TPEPy-PF6** with 99.67% water content.

system. Based on this observation, it is reasonable to expect that $^1O_2$ might be possibly generated by the oxidation of $\bullet O_2^-$ as illustrated in Fig. 4. From the molecular orbital diagram (Fig. 4), it is evident that the loss of an electron of appropriate spin could generate either $^1O_2$ or $^3O_2$. The probabilities of $^1O_2$ and $^3O_2$ production through the oxidation of $\bullet O_2^-$ are found to be 2/5 and 3/5, respectively [37]. The confirmation of the production of $\bullet O_2^-$ also indicates the possibility of the generation of other types of ROS as well because $\bullet O_2^-$ is the precursor of most of the ROS and is a mediator of oxidative chain reactions [44]. It is worthwhile to mention that the increase in RNO absorbance at 440 nm of DI water + BQ +10 W group (black curve in Fig. 3d) is due to the interaction of imidazole with BQ [45]. As can be seen in Fig. S5a, the absorption of RNO at 440 nm did not change in the presence of BQ, indicating that RNO does not interact with BQ. However, the absorption of RNO at 440 nm slightly increased in the presence of imidazole and BQ (Fig. S5c), which suggests that imidazole interacts with BQ as discussed in the literature [45]. Fig. S5d further shows that the interaction becomes more prominent upon MW irradiation.

We also used another scavenger of $\bullet O_2^-$, chloroform [43,46,47], to further strengthen our claim that the nanoaggregates can generate $\bullet O_2^-$ upon MW radiation. After adding chloroform (4.2 or 21 mM) to **TPEPy-I** solution, the bleaching of RNO was noticeably reduced (Fig. S6a),

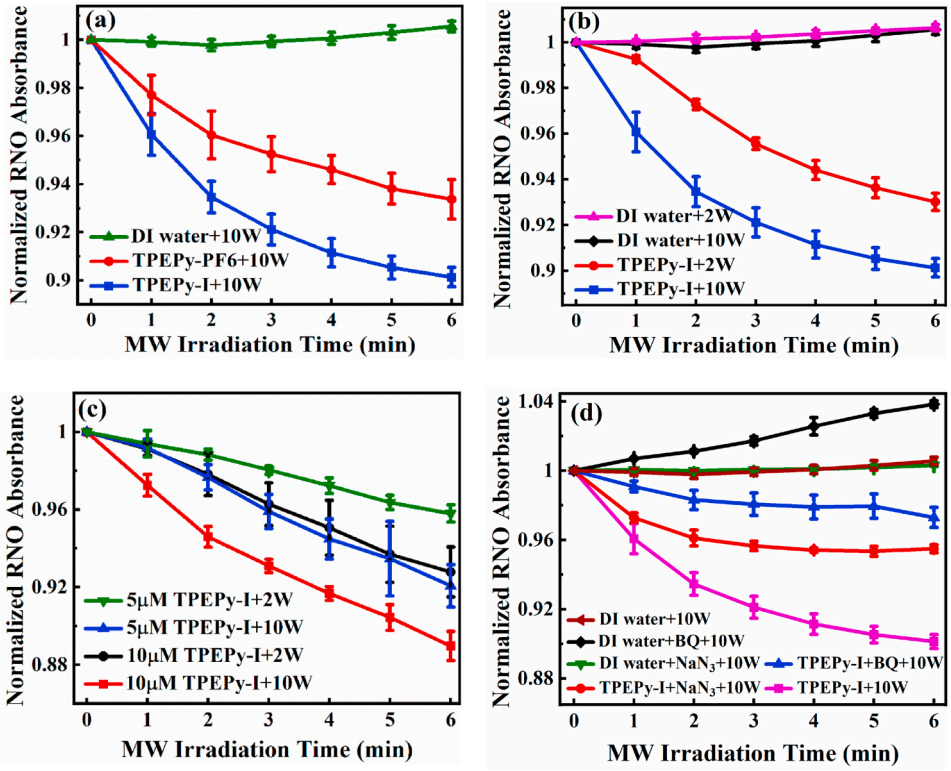

Fig. 3. Investigation of ROS detection using the RNO bleaching (RNO-imidazole) method. Normalized absorption curves of RNO at 440 nm in the presence of (a) DI water, **TPEPy-I**, or **TPEPy-PF6** under 10 W of MW irradiation, (b) DI water or **TPEPy-I** under 2 and 10 W of MW irradiation, (c) **TPEPy-I** (5 and 10 μM) under 2 and 10 W of MW irradiation, and (d) DI water, BQ, NaN_3, **TPEPy-I**, **TPEPy-I** + NaN_3, or **TPEPy-I** + BQ under 10 W of MW irradiation.

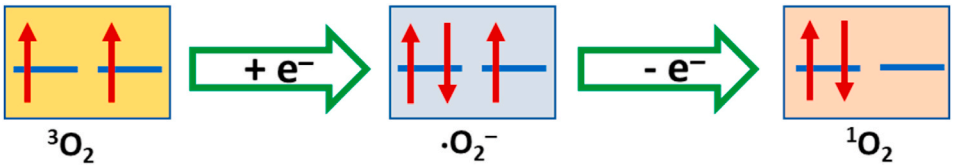

Fig. 4. The schematic molecular π* orbitals of molecular oxygen ($^3O_2$), superoxide radical ($\bullet O_2^-$), and singlet oxygen ($^1O_2$).

indicating that the nanoaggregates could produce $\bullet O_2^-$ under MW irradiation.

Additionally, the absorbance of RNO was also monitored without using imidazole to further affirm the production of $^1O_2$ (Fig. S6b). If the system generates $^1O_2$, the bleaching of RNO should reduce in the absence of imidazole. As expected, the bleaching of RNO was significantly inhibited in the absence of imidazole as compared to the sample with imidazole (Fig. S6b), further demonstrating that the sample can generate $^1O_2$ upon MW exposure.

For the purpose of comparison, we synthesized copper-cysteamine (Cu-Cy) nanoparticles using the recently published method [19] and compared the ROS production performance of **TPEPy-I** nanoaggregates (10 μM) with Cu-Cy nanoparticles (10 μM) under the same experimental conditions. As depicted in Fig. S7, **TPEPy-I** nanoaggregates produced a significantly higher amount of ROS than that of Cu-Cy nanoparticles, justifying that **TPEPy-I** nanoaggregates are better ROS producing agent than Cu-Cy nanoparticles upon MW irradiation.

3.4. Study of $^1O_2$ measurements using ABDA probe and electron spin resonance (ESR) spectroscopy

The generation of $^1O_2$ from the two nanoaggregates upon MW irradiation was also assessed by using ABDA, a commercially available $^1O_2$ indicator [30]. ABDA can react with $^1O_2$ to form an endoperoxide, resulting in a decrease in the absorbance of ABDA. As indicated in Fig. 5a, a slight reduction in the absorbance of ABDA was observed even in the absence of the samples, signifying that MW alone caused some oxidation of ABDA. In contrast, after adding **TPEPy-I** or **TPEPy-PF6** (15 μM) to the ABDA solution, a rapid decrease in the intensity of ABDA absorbance was noticed with increasing the MW exposure time (Fig. 5a), which is an indication of $^1O_2$ generation and provided compelling evidence of $^1O_2$ production. As expected, **TPEPy-I** nanoaggregates exhibited a much more effective $^1O_2$ generation, consistent with what was observed during the RNO bleaching assay.

As **TPEPy-I** generated more $^1O_2$, we further measured $^1O_2$ produced by **TPEPy-I** (15 μM) upon 2 W of MW radiation. The results presented in Fig. 5b reveal that $^1O_2$ produced by **TPEPy-I** varies with MW power. To validate that decrease in ABDA absorbance was due to the generation of $^1O_2$, we mixed DABCO, a well-known scavenger of $^1O_2$ [36], to the solution of **TPEPy-I** (15 μM). As displayed in Fig. 5c, the decrease in ABDA absorbance was markedly inhibited in the presence of the DABCO (20 mM), further testifying that the **TPEPy-I** nanoaggregates could generate $^1O_2$ upon MW exposure.

To examine whether the molecularly dissolved state can produce $^1O_2$ upon MW excitation, we chose **TPEPy-I** as an example for further investigation. Fig. 5d reveals that **TPEPy-I** solution could not induce $^1O_2$ in the molecular form (0% water). Surprisingly, no obvious $^1O_2$ generation was observed even when the water content was 66.67%. However,

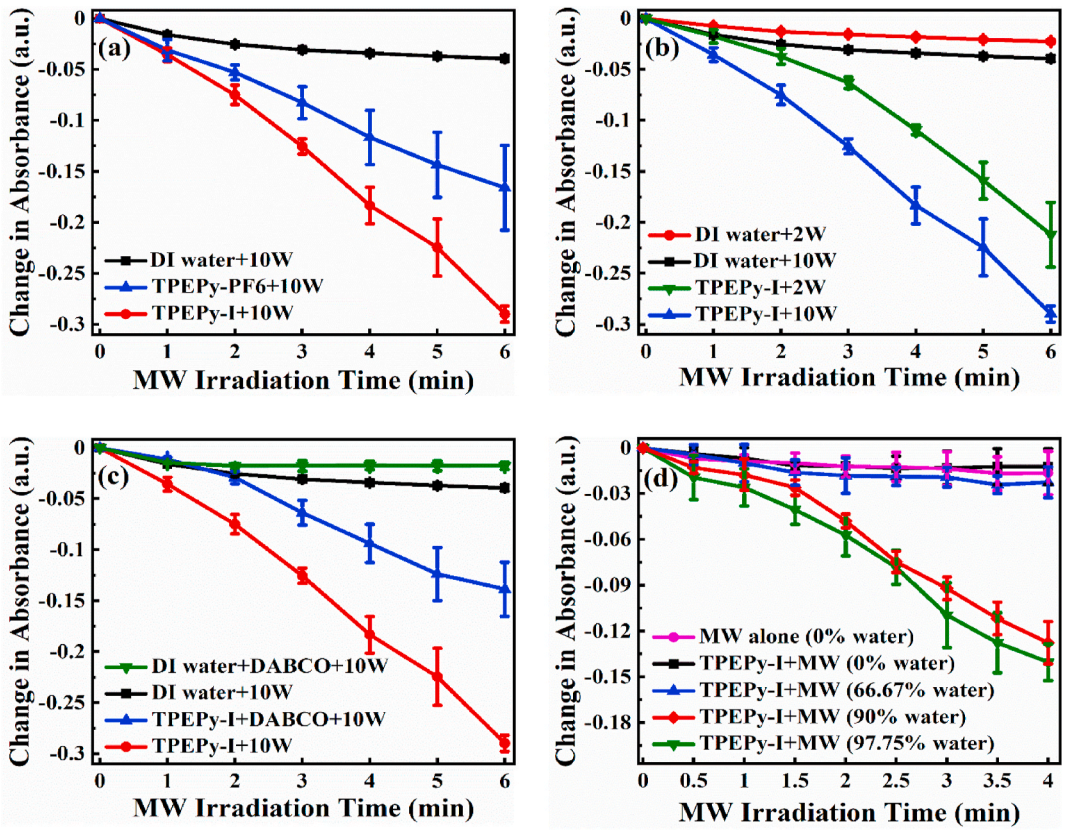

Fig. 5. Exploration of singlet oxygen ($^1O_2$) detection using the ABDA probe. Change in ABDA absorbance at 379 nm as a function of MW exposure time with (a) **TPEPy-I** or **TPEPy-PF6** nanoaggregates under 10 W of MW irradiation, (b) **TPEPy-I** nanoaggregates under 2 and 10 W of MW irradiation, (c) DABCO, **TPEPy-I** + DABCO, or **TPEPy-I** under 10 W of MW irradiation, and (d) **TPEPy-I** in the presence of different water contents in DMF under 10 W of MW irradiation. The decrease in absorbance at 379 nm shows $^1O_2$ production.

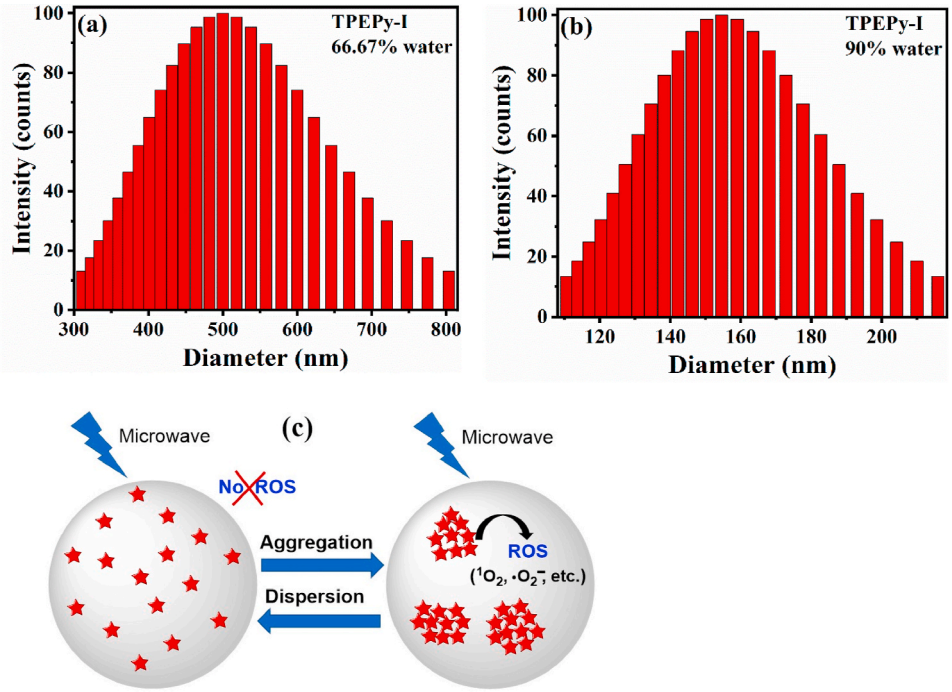

Fig. 6. The particle size distribution of nanoaggregates of **TPEPy-I** formed in DMF-water mixture with (a) 66.67% and (b) 90% water content measured by DLS. The average hydrodynamic diameters were found to be (517 ± 108) and (157 ± 24) nm, respectively. (c) Schematic diagram of the AIEgen-mediated microwave dynamic therapy (MWDT).

further increasing water content (90% or 97.75%), **TPEPy-I** generated a large amount of $^1O_2$. All of these findings indicate that MW can generate $^1O_2$ only when compact nanoaggregates are formed, as demonstrated by DLS measurements (Fig. 6a and b). The AIEgen-mediated MWDT is schematically illustrated in Fig. 6c.

ESR technique was used to further verify the production of $^1O_2$ using 2,2,6,6-tetramethylpiperidine (TEMP), a well-known probe molecule for trapping $^1O_2$. The oxidation of TEMP by $^1O_2$ yields the stable free radical 2,2,6,6-tetramethyl-1-piperidinyloxy (TEMPO), which can be easily detected by ESR [48,49]. As shown in Fig. 7, the distinguishable and typical 1:1:1 triplet signal (i.e., three lines with equal intensities) of the TEMPO was detected after applying MW irradiation on **TPEPy-I** nanoaggregates (10 μM), thereby providing direct evidence of the generation of $^1O_2$ [48,49]. However, such a noticeable characteristic signal of the TEMPO was not observed without MW irradiation. Similarly, we conducted experiments on **TPEPy-PF6** nanoaggregates to see if **TPEPy-PF6** nanoaggregates (10 μM) could produce $^1O_2$, and results showed that **TPEPy-PF6** nanoaggregates could generate $^1O_2$ when excited by MW (Fig. 7). Additionally, $^1O_2$ produced by **TPEPy-I** nanoaggregates was more than that of **TPEPy-PF6**, consistent with all our studies.

3.5. Detection of extracellular ROS production using DCFH-DA probe

The evaluation of ROS generation was also explored by the PL technique using DCFH-DA, which yields DCF, a fluorescent molecule, in the presence of ROS [8,23]. As shown in Fig. 8a, it is evident that the PL intensity at 523 nm enhanced to a greater extent after using **TPEPy-I** or **TPEPy-PF6** nanoaggregates when compared to the DI water alone, demonstrating that the **TPEPy-I** and **TPEPy-PF6** nanoaggregates can produce ROS upon MW exposure. Taking **TPEPy-I** as an example, we further evaluated the ROS produced by the **TPEPy-I** nanoaggregates at 2 and 5 W of MW irradiation. The results presented in Fig. S8 demonstrate that the nanoaggregates could produce ROS even at 2 W of MW irradiation. For comparison, Fig. 8b was plotted, which shows that ROS production ability enhanced with the increase of MW power.

3.6. Intracellular ROS detection

The results of ROS production in cell-free system motivated us to explore ROS detection in cells. DCFH-DA, an oxidation-sensitive probe, was used to examine the intracellular ROS generation. DCFH-DA is a nonpolar and cell-permeant compound, which switches to DCFH by intracellular esterases and then converts to the intensely fluorescent DCF upon oxidation with intracellular ROS [31]. The representative images presented in Fig. 9 demonstrate that negligible green fluorescence was seen in the MW (1 or 1.5 min, 10 W) treated cells, whereas the cells treated with **TPEPy-I** or **TPEPy-PF6** nanoaggregates (5 μM) displayed weakly green fluorescence. Meanwhile, the intensity of green fluorescence was dramatically increased in the cells treated with the **TPEPy-I** or **TPEPy-PF6** nanoaggregates in combination with MW, proving that the two nanoaggregates can remarkably produce ROS when stimulated by MW. Additionally, the intensity of green fluorescence was further enhanced after increasing the MW exposure time from 1 to 1.5 min. These findings also support that the two AIEgens can produce ROS under MW exposure and are promising sensitizers for MWDT.

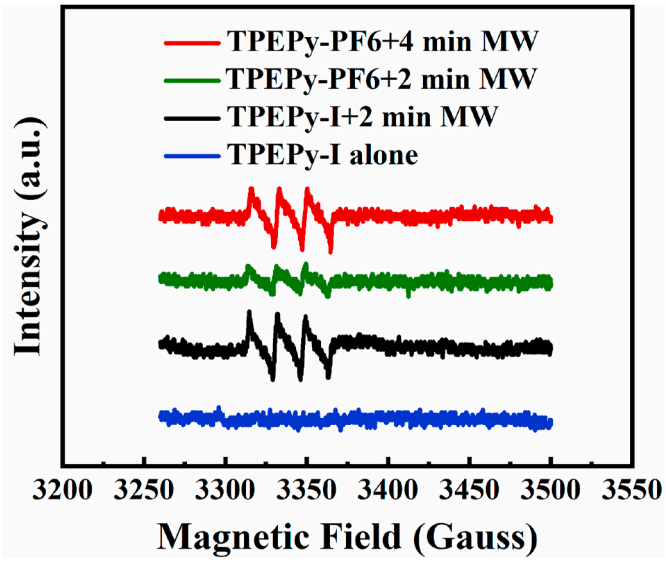

Fig. 7. ESR spectra of $^1O_2$ trapped by TEMP in the presence of **TPEPy-I** and **TPEPy-PF6** nanoaggregates (10 μM) under 10 W of MW irradiation. Concentration of TEMP was 20 mM.

3.7. Exploration of MWDT effect using MTT assay

We evaluated the MWDT effect of the two AIEgens using MTT assay. It is a quantitative colorimetric assay in which yellow tetrazolium salt MTT converts into purple formazan crystals by mitochondrial dehydrogenase of the metabolically active cells [50]. The results presented in Fig. 10 shows that MW-treated nanoaggregates killed significantly more cells than their corresponding controls (MW alone and nanoaggregates alone). Furthermore, our results depict that the lethality increased with the increase of concentration of **TPEPy-I** and **TPEPy-PF6** nanoaggregates, demonstrating a dose-dependent cytotoxic effect. These results confirmed that the combination of MW and **TPEPy-I** or **TPEPy-PF6** nanoaggregates had a fatal effect on HeLa cells. For example, the average HeLa cell viabilities were found to be 58.4% vs. 62.5%, 31.1% vs. 36.7%, and 9.3% vs. 14.2% at 2.5, 5, and 10 μM of **TPEPy-I** and **TPEPy-PF6** nanoaggregates, respectively, under 10 W of MW irradiation for 1.5 min. Even though it may not be fully reasonable to compare our findings with the reported results due to some differences in the experimental methods, the high MWDT effect of the two AIEgens even at low concentration indicates that the present AIEgen system is better than most MW sensitizers reported thus far, which require high concentrations to achieve the desired cytotoxicity [18–25].

The IC-50 values of **TPEPy-I** and **TPEPy-PF6** nanoaggregates upon MW were found to be (2.73 ± 0.52) and (3.22 ± 0.55) μM, respectively (Fig. 11). This means that **TPEPy-I** nanoaggregates showed a better MWDT effect on average, which agrees with the ROS production and cytotoxicity studies.

The toxicity of materials is a very important factor to be evaluated for biological applications. Therefore, we further assessed the dark toxicity of the two nanoaggregates in both normal and cancer cells (other than HeLa cancer cells). As displayed in Fig. 12, the nanoaggregates have relatively low dark toxicity in both cancer and normal cells up to tested concentrations. Additionally, the average dark toxicity for HET1A (normal cells) for most concentrations was found to be slightly lower than that of KYSE-30 (cancer cells). These results suggest that these nanoaggregates should have acceptable biocompatibility in normal cells *in vivo*.

3.8. MWDT study by live/dead assay

The anti-tumor effect induced by **TPEPy-I** and **TPEPy-PF6** nanoaggregates upon MW exposure was also assessed by using the live/dead cell viability assay. HeLa cells were stained with calcein-AM for viable cells and PI for nonviable cells. Calcein-AM is a cell-permeable dye that has been widely employed for determining cell viability and/or cytotoxicity in most eukaryotic cells. In viable cells, the calcein-AM is switched to a green fluorescent calcein by intracellular esterases [51]. On the other hand, PI is excluded from live cells with intact plasma membranes but penetrates damaged cells, thereby binding to nucleic acids and detecting dead cells in a population [31].

For each group, the green (live) and red (dead) channels were

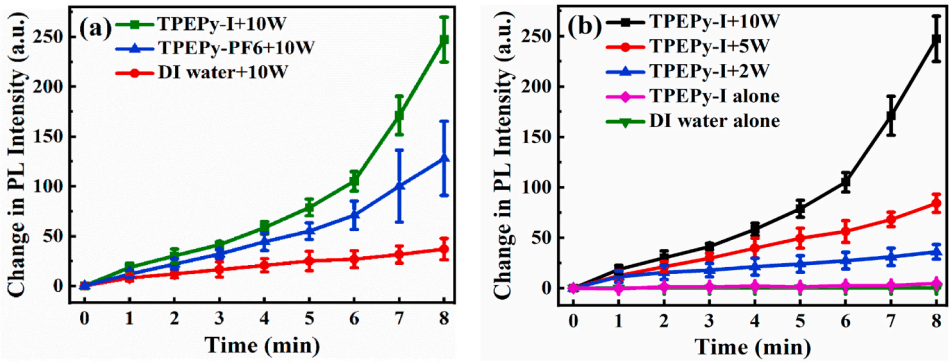

Fig. 8. Extracellular ROS detection using the DCFH-DA probe. (a) Change in photoluminescence (PL) intensities of DCF at 523 nm as a function of MW exposure time with or without **TPEPy-I** and **TPEPy-PF6** nanoaggregates (10 μM) under 10 W of MW irradiation. (b) Comparison of change in PL intensities of DCF at 523 nm in the presence of **TPEPy-I** nanoaggregates (10 μM) at 2, 5, and 10 W of MW irradiation. The increase in PL intensity at 523 nm indicates the ROS generation.

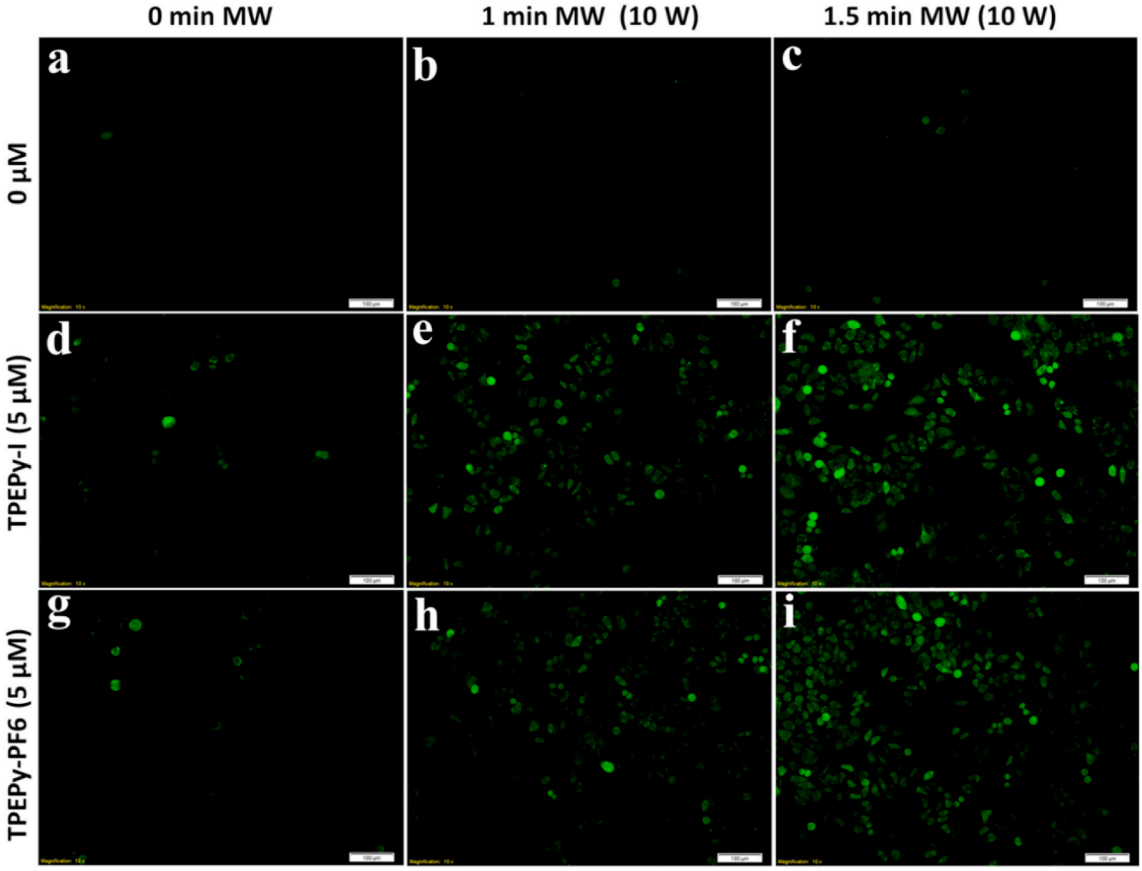

Fig. 9. Intracellular ROS detection in HeLa cells using DCFH-DA staining dye upon 10 W of MW irradiation. (a) Cells without any treatments. (b) Cells treated with MW for 1 min. (c) Cells treated with MW for 1.5 min. (d) Cells treated with **TPEPy-I**. (e) Cells treated with **TPEPy-I** upon MW for 1 min. (f) Cells treated with **TPEPy-I** upon MW for 1.5 min. (g) Cells treated with **TPEPy-PF6**. (h) Cells treated with **TPEPy-PF6** upon MW for 1 min, and (i) cells treated with **TPEPy-PF6** upon MW for 1.5 min. The increase in green fluorescence intensity shows ROS production. Scale bar = 100 μm; magnification = 10 × .

merged, and the representative images of the live/dead assay are shown in Fig. 13. When **TPEPy-I** or **TPEPy-PF6** nanoaggregates were activated by 1.5 or 2 min of MW (10 W), the cytotoxicity was significantly enhanced when compared to their corresponding controls (MW alone and nanoaggregates alone). The results presented in Fig. 13 further show that more cells were destroyed while increasing the MW exposure time (from 1.5 to 2 min), uncovering that **TPEPy-I** and **TPEPy-PF6** nanoaggregates are promising candidates in MWDT for noninvasive treatment of deep tumors and infectious diseases. For the purpose of quantification, the number of live (green fluorescence) and dead (red fluorescence) cells were counted to determine the cell viability by using ImageJ software [52], and the results are displayed in Fig. 14. The average cell viabilities of the HeLa cells in the presence of **TPEPy-I** and **TPEPy-PF6** nanoaggregates under 10 W of MW exposure were found to be 23.8% and 29.1% for 1.5 min and 4.7% and 7.5% for 2 min, respectively (Fig. 14). Again, this means that **TPEPy-I** nanoaggregates exhibited a better MWDT outcome on average than **TPEPy-PF6** nanoaggregates, which could be due to the effect of iodide ions, as pointed out in our recent publication [34].

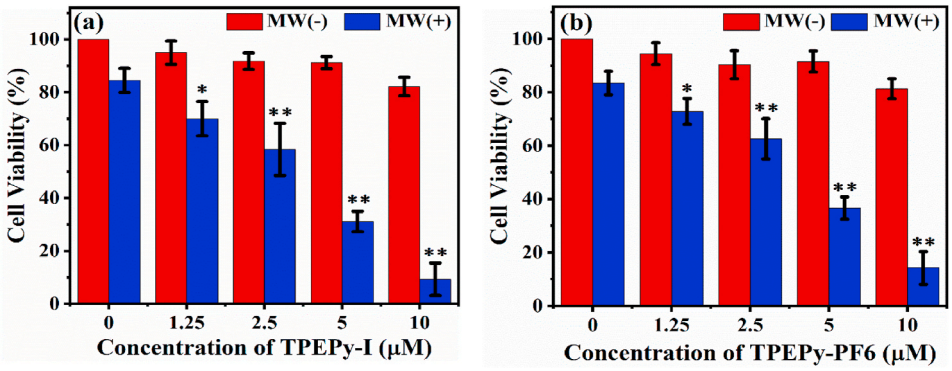

Fig. 10. Evaluation of MWDT effect of (a) **TPEPy-I** and (b) **TPEPy-PF6** nanoaggregates under MW irradiation (10 W) on HeLa cells for 1.5 min. Statistical analysis was performed with respect to MW alone and the corresponding concentration of the nanoaggregate alone (*$p < 0.05$ and **$p < 0.0001$).

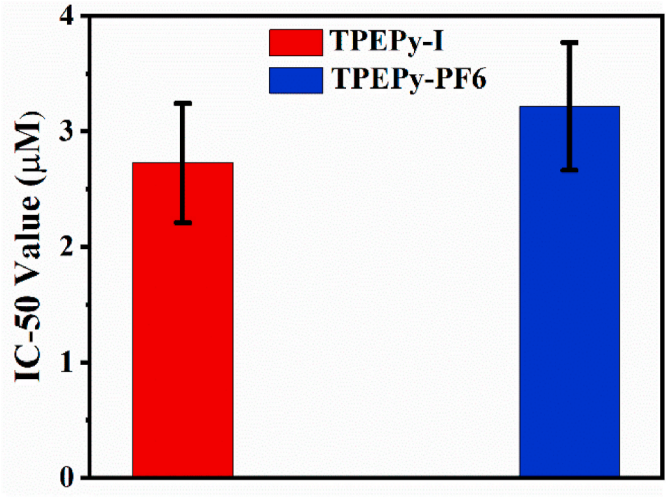

Fig. 11. The plot of IC-50 values of **TPEPy-I** and **TPEPy-PF6** nanoaggregates against HeLa cells under 10 W (1.5 min) of MW exposure.

3.9. Bright-field images

We also monitored the changes in the morphology of the HeLa cells following the MW treatments. As shown in Fig. 15, the cells treated with **TPEPy-I** nanoaggregates alone retained their regular and normal cell morphology, indicating low dark cytotoxicity towards HeLa cells. In contrast, MW plus nanoaggregates induced a dramatic change in cell morphology, thus corroborating that the combination of the nanoaggregates and MW is highly toxic to cancer cells. The results agreed well with the results of the MTT and live/dead assays.

3.10. ROS production and MW heating

Despite several groups, including ours, great efforts in elucidating the mechanisms of MW induced ROS generation, the exact mechanism is not completely understood yet because MW irradiation does not have sufficient energy to break chemical bonds or to induce any chemical reactions [23,28]. One of the plausible rationalities is that a portion of MW energy could be concentrated into hot spots, which could cause the transfer of electrons from the nanoaggregates to the surrounding water and oxygen, thereby producing ROS [23,53]. Another possibility could be attributed to the catalytic effect of the nanoaggregates, similar to that of other materials such as Cu-Cy nanoparticles [19], g-C_3N_4 quantum dots [20], gold nanoparticles [26], and activated carbon [53]. Additionally, non-thermal effect of MW may cause excitation of reactant molecules to higher vibrational and rotational energy levels [54–56]. Shahin et al. [57] discussed that the non-thermal effect of MW could be responsible for increasing ROS production. Although the exact mechanism of ROS production is still controversial, it is well accepted that MW irradiation forces polar molecules to continuously realign with the oscillating electric field, enhancing their kinetic energy and, in turn, heat [15,28]. Tissues with high water content (such as solid organs and tumors) are highly conducive to this type of heating [15]. Increasing evidence support that heat can mediate for ROS production, including $^1O_2$ [31,58,59].

To determine whether MW irradiation can produce $^1O_2$ through the dismutation of hydrogen peroxide (H_2O_2), we employed singlet oxygen sensor green (SOSG) reagent, which can react with $^1O_2$ and emit bright green fluorescence peaked at about 525 nm [60]. When H_2O_2 (100 μM)

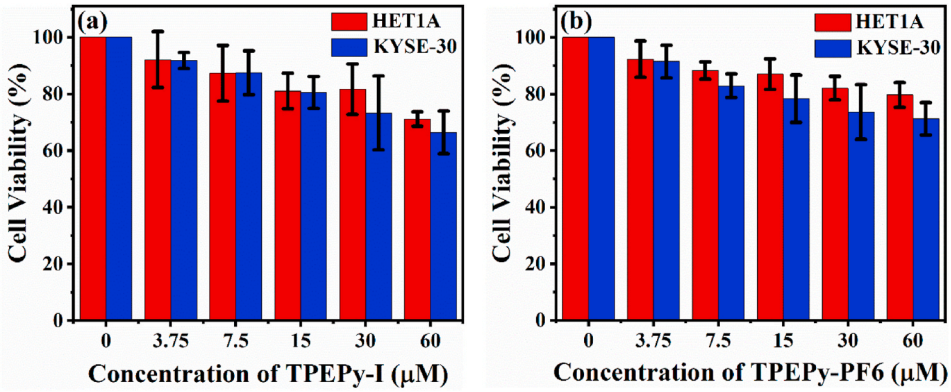

Fig. 12. Cell viability of HET1A normal cells and KYSE-30 cancer cells under the dark condition after treating different concentrations of (a) **TPEPy-I** and (b) **TPEPy-PF6** nanoaggregates for 24 h.

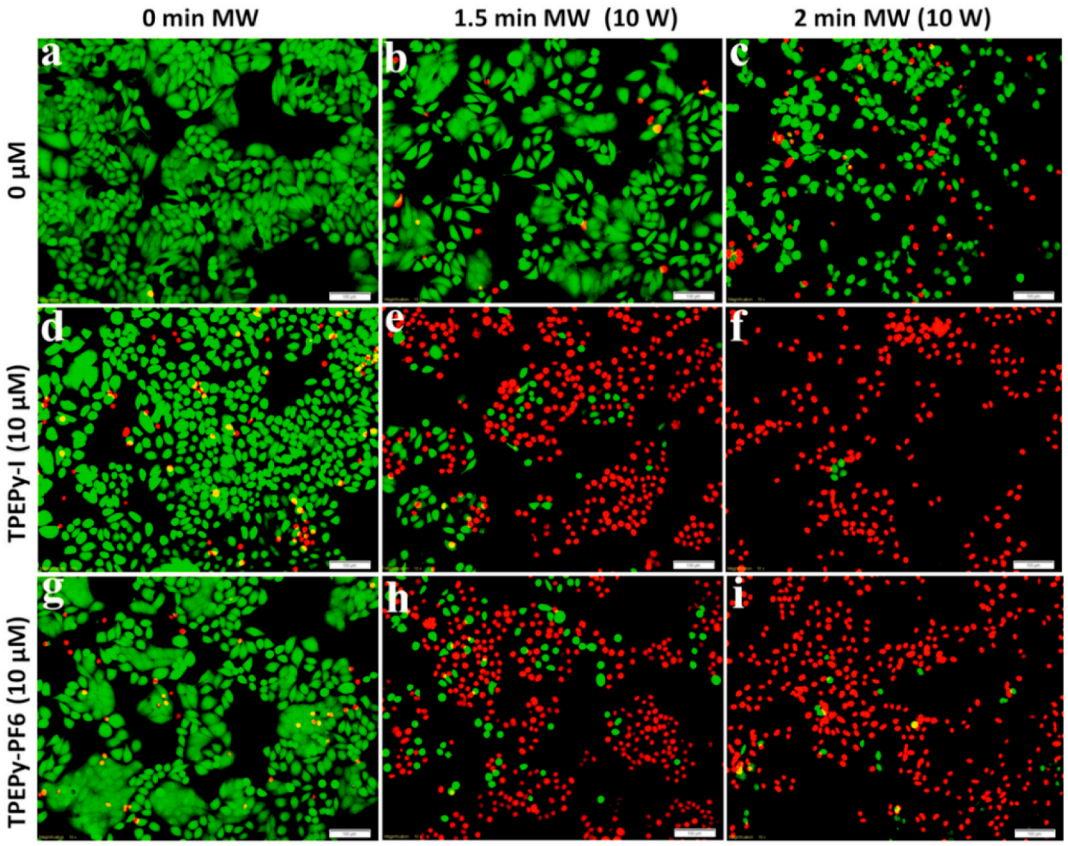

Fig. 13. The effect of **TPEPy-I** and **TPEPy-PF6** nanoaggregates (10 μM) in HeLa cells upon 10 W of MW irradiation. (a) Cells without any treatments. (b) Cells treated with MW for 1.5 min. (c) Cells treated with MW for 2 min. (d) Cells treated with **TPEPy-I**. (e) Cells treated with **TPEPy-I** upon MW for 1.5 min. (f) Cells treated with **TPEPy-I** upon MW for 2 min. (g) Cells treated with **TPEPy-PF6**. (h) Cells treated with **TPEPy-PF6** upon MW for 1.5 min, and (i) cells treated with **TPEPy-PF6** upon MW for 2 min. Green fluorescence represents viable cells, whereas red fluorescence represents dead cells. Scale bar = 100 μm; magnification = 10 × .

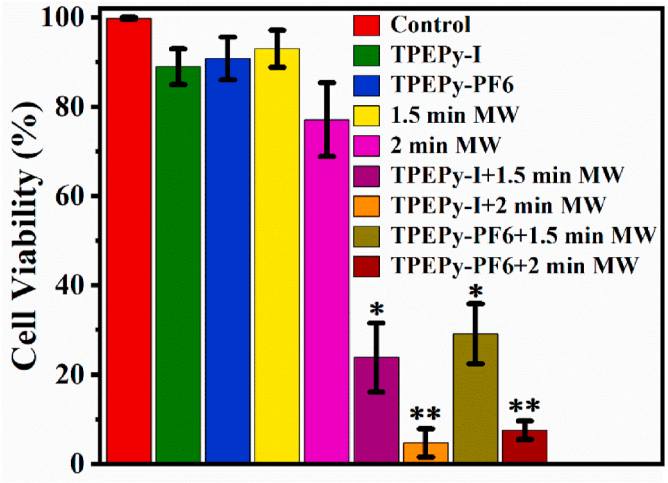

Fig. 14. The quantitative analysis of the live/dead cell assay using ImageJ software. *$p < 0.0001$ compared with 1.5 min MW alone and the corresponding nanoaggregate alone; **$p < 0.00001$ compared with 2 min MW alone and the corresponding nanoaggregate alone.

was stimulated by MW (2 and 10 W), the normalized PL intensity at 525 nm enhanced remarkably as compared to H_2O_2 alone and MW alone in both time- and dose-dependent manners (Fig. 16a), thereby providing strong evidence that MW can generate $^1O_2$ by decomposing H_2O_2. In fact, ROS production by MW is a common phenomenon, which has been reported as a great concern for mobile phone impact on human health due to their increased use in daily life [61–63].

To elucidate the heating effect of MW, temperatures of DI water with or without the two nanoaggregates were recorded at 10 W of MW irradiation (2450 MHz) up to 6 min. As displayed in Fig. 16b, the temperature of the DI water in the presence of **TPEPy-I** or **TPEPy-PF6** nanoaggregates (20 μM) was not higher than in the DI water alone, suggesting MW thermal effect is unlikely to be a major factor for killing cancer cells and excluding the possibility that these nanoaggregates may increase the temperature of MW heating. Based on this observation and our findings as described above, it is reasonable to expect that the destruction of cancer cells is primarily due to ROS, and, therefore, we define it microwave dynamic therapy (MWDT).

It is known that photodynamic therapy (PDT) suffers from a key drawback associated with its oxygen-dependent nature, which limits its effective use against hypoxic tumors [64,65]. Many strategies have been explored to solve this problem and improving blood flow in tumors is one of them [64]. Since tumor hypoxia is particularly caused by the alterations in tumor microenvironments and the chaotic blood flow, improving blood flow has become an effective approach to increase oxygenation in tumors. It has been reported that elevating local temperatures by a mild heating may increase blood flow in tumors and an increment of the oxygen level inside tumor [64]. Therefore, microwave induced photodynamic therapy with the microwave heating along with the dynamic therapy of ROS is a good combination on cancer treatment, not only improve the efficacy but also could provide a good solution for hypoxic issues.

4. Conclusions

For the first time, we presented that two AIEgens (**TPEPy-I** and

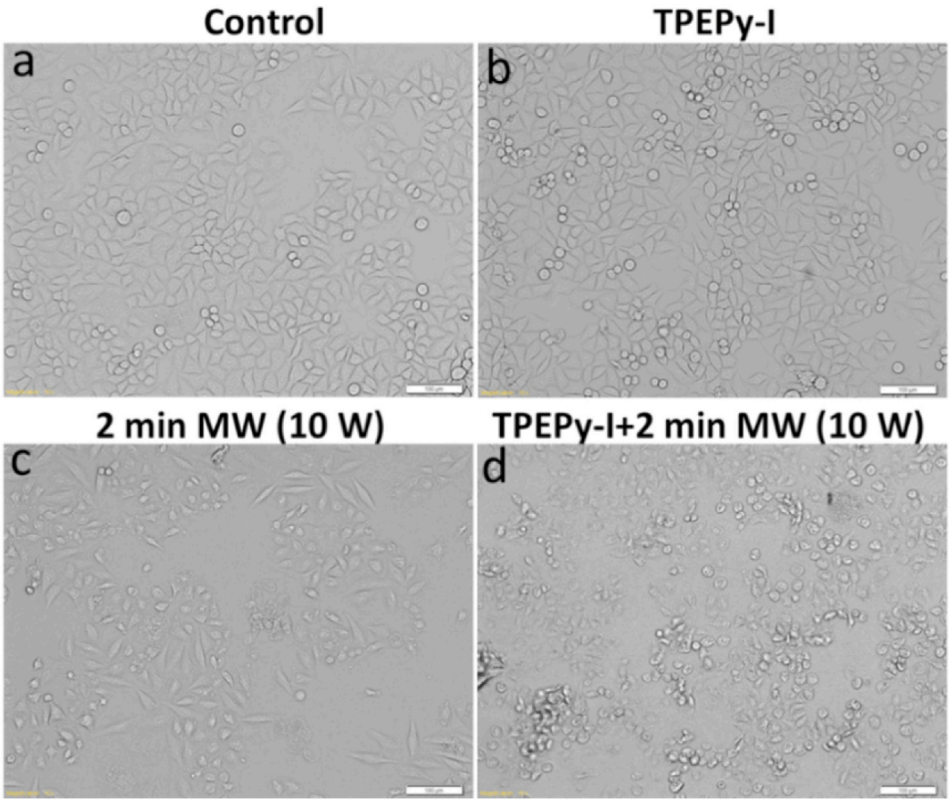

Fig. 15. Bright-field images of HeLa cells (a) without any treatments (control), (b) treated with **TPEPy-I** (10 μM), (c) treated with MW for 2 min, and (d) treated with **TPEPy-I** (10 μM) upon MW for 2 min. Scale bar = 100 μm; magnification = 10 × .

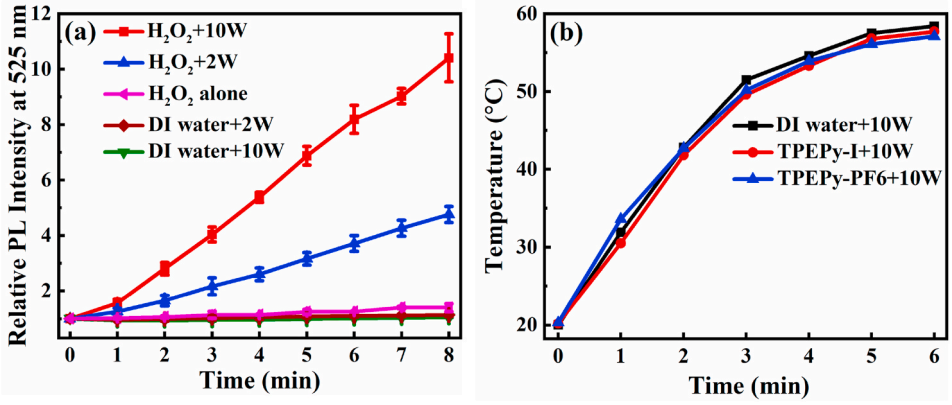

Fig. 16. (a) The relative PL intensity of SOSG at 525 nm with or without H_2O_2 (100 μM) as a function of time upon 2 and 10 W of MW irradiation. The increase in PL intensity at 525 nm represents the $^1O_2$ generation. The excitation wavelength was 505 nm. (b) *In vitro* MW heating curves of **TPEPy-I** and **TPEPy-PF6** nanoaggregates dispersed in DI water upon 10 W of MW irradiation. DI water was set as a control.

TPEPy-PF6) can produce ROS and, in turn, kill cancer cells under MW irradiation. We employed different methods to affirm that the two AIEgens can induce ROS upon MW exposure. The AIEgens showed significant cytotoxicity when excited by MW toward HeLa cells as evaluated by the MTT and live/dead assays. Considering NIR emission, good stability, and effectiveness for killing cancer cells even under low concentration of **TPEPy-I** or **TPEPy-PF6** nanoaggregates, we anticipate that these nanoaggregates could be deserving candidates for further investigation in the study of image-guided MWDT, either alone or in combination with other treatment modalities, such as radiotherapy, chemotherapy, immunotherapy, or surgery. This novel work opens a new door to provide an effective perspective on the molecular design of AIEgens to approach clinical application and improve the efficacy of cancer treatments.

Conflicts of interest

There are no conflicts to declare.

CRediT authorship contribution statement

Nil Kanatha Pandey: Methodology, Synthesis, Cell Studies, Characterization, Microscope and AFM images, Writing – original draft. **Wei Xiong:** Methodology, Synthesis, Cell Studies, Characterization. **Lingyun Wang:** Conceptualization, Instruction, Funding acquisition, Writing – original draft. **Wei Chen:** Conceptualization, Instruction, Funding

acquisition, Writing – original draft. **Brian Bui:** Formal analysis, Data curation, Writing – review & editing. **Jian Yang:** Conceptualization, Instruction, Funding acquisition, Writing – original draft. **Eric Amador:** Writing – original draft. **Mingli Chen:** Formal analysis, Data curation, Writing – review & editing. **Christina Xing:** Formal analysis, Data curation, Writing – review & editing. **Aseem Atul Athavale:** Formal analysis, Data curation, SEM measurements. **Yaowu Hao:** Formal analysis, Data curation, SEM measurements. **Wirya Feizi:** Formal analysis, ESR measurements. **Lloyd Lumata:** Formal analysis, ESR measurements.

Declaration of competing interest

The authors declare that they have no known competing financial interests or personal relationships that could have appeared to influence the work reported in this article.

Acknowledgments

We would like to acknowledge the supports from Guangxi Jialouyuan Medical Inc., Solgro, and the distinguished award from UT Arlington, the Pencis award, as well as the supports from the China Scholarship Council (201906155012), the National Natural Science Foundation of China (22071065, 21772045), the Natural Science Foundation of Guangdong Province (2018B030311008), and the Technology Program of Guangzhou (201904010414). We would also like to acknowledge Dr. Kytai Nguyen for helping with DLS measurements and Alexios Papadimitratos for ESR measurements. LL would like to acknowledge support by the Welch Foundation grant number AT-1877-20180324 and the UT Dallas-NRUF Collaborative Biomedical Research Award (CoBRA).

Appendix A. Supplementary data

Supplementary data to this article can be found online at https://doi.org/10.1016/j.bioactmat.2021.05.031.

References

[1] Á. Juarranz, P. Jaén, F. Sanz-Rodríguez, J. Cuevas, S. González, Photodynamic therapy of cancer. Basic principles and applications, Clin. Transl. Oncol. 10 (3) (2008) 148–154.
[2] S. Li, L. Tan, X. Meng, Nanoscale metal-organic frameworks: synthesis, biocompatibility, imaging applications, and thermal and dynamic therapy of tumors, Adv. Funct. Mater. 30 (13) (2020), 1908924.
[3] L. Chudal, N.K. Pandey, J. Phan, O. Johnson, X. Li, W. Chen, Investigation of PPIX-Lipo-MnO_2 to enhance photodynamic therapy by improving tumor hypoxia, Mater. Sci. Eng. C 104 (2019), 109979.
[4] J. Mei, N.L. Leung, R.T. Kwok, J.W. Lam, B.Z. Tang, Aggregation-induced emission: together we shine, united we soar!, Chem. Rev. 115 (21) (2015) 11718–11940.
[5] M. Li, Y. Gao, Y. Yuan, Y. Wu, Z. Song, B.Z. Tang, B. Liu, Q.C. Zheng, One-step formulation of targeted aggregation-induced emission dots for image-guided photodynamic therapy of cholangiocarcinoma, ACS Nano 11 (4) (2017) 3922–3932.
[6] M. Gao, B.Z. Tang, AIE-based cancer theranostics, Coord. Chem. Rev. 402 (2020), 213076.
[7] J. Qian, B.Z. Tang, AIE luminogens for bioimaging and theranostics: from organelles to animals, Chem 3 (1) (2017) 56–91.
[8] Z. Liu, H. Zou, Z. Zhao, P. Zhang, G.-G. Shan, R.T. Kwok, J.W. Lam, L. Zheng, B. Z. Tang, Tuning organelle specificity and photodynamic therapy efficiency by molecular function design, ACS Nano 13 (10) (2019) 11283–11293.
[9] M. Yang, J. Li, P. Gu, X. Fan, The application of nanoparticles in cancer immunotherapy: targeting tumor microenvironment, Bioact. Mater. 6 (7) (2021) 1973–1987.
[10] K.F. Chu, D.E. Dupuy, Thermal ablation of tumours: biological mechanisms and advances in therapy, Nat. Rev. Canc. 14 (3) (2014) 199–208.
[11] M. Yang, T. Yang, C. Mao, Enhancement of photodynamic cancer therapy by physical and chemical factors, Angew. Chem. Int. Ed. 58 (40) (2019) 14066–14080.
[12] A.J. Moy, J.W. Tunnell, Combinatorial immunotherapy and nanoparticle mediated hyperthermia, Adv. Drug Deliv. Rev. 114 (2017) 175–183.
[13] H.A. Albarqi, L.H. Wong, C. Schumann, F.Y. Sabei, T. Korzun, X. Li, M.N. Hansen, P. Dhagat, A.S. Moses, O. Taratula, Biocompatible nanoclusters with high heating efficiency for systemically delivered magnetic hyperthermia, ACS Nano 13 (6) (2019) 6383–6395.
[14] X. Zhang, J. Tang, C. Li, Y. Lu, L. Cheng, J. Liu, A targeting black phosphorus nanoparticle based immune cells nano-regulator for photodynamic/photothermal and photo-immunotherapy, Bioact. Mater. 6 (2) (2021) 472–489.
[15] M.G. Lubner, C.L. Brace, J.L. Hinshaw, F.T. Lee Jr., Microwave tumor ablation: mechanism of action, clinical results, and devices, J. Vasc. Intervent. Radiol. 21 (8 Suppl) (2010) S192–S203.
[16] C.J. Simon, D.E. Dupuy, W.W. Mayo-Smith, Microwave ablation: principles and applications, Radiographics 25 (suppl_1) (2005) S69–S83.
[17] H. Shi, T. Liu, C. Fu, L. Li, L. Tan, J. Wang, X. Ren, J. Ren, J. Wang, X. Meng, Insights into a microwave susceptible agent for minimally invasive microwave tumor thermal therapy, Biomaterials 44 (2015) 91–102.
[18] M. Yao, L. Ma, L. Li, J. Zhang, R. Lim, W. Chen, Y. Zhang, A new modality for cancer treatment–nanoparticle mediated microwave induced photodynamic therapy, J. Biomed. Nanotechnol. 12 (10) (2016) 1835–1851.
[19] N.K. Pandey, L. Chudal, J. Phan, L. Lin, O. Johnson, M. Xing, J.P. Liu, H. Li, X. Huang, Y. Shu, W. Chen, A facile method for the synthesis of copper-cysteamine nanoparticles and study of ROS production for cancer treatment, J. Mater. Chem. B 7 (42) (2019) 6630–6642.
[20] X. Chu, K. Li, H.Y. Guo, H.B. Zheng, S. Shuda, X.L. Wang, J.Y. Zhang, W. Chen, Y. Zhang, Exploration of graphitic-C_3N_4 quantum dots for microwave-induced photodynamic therapy, ACS Biomater. Sci. Eng. 3 (8) (2017) 1836–1844.
[21] X. Chu, L. Mao, O. Johnson, K. Li, J. Phan, Q. Yin, L. Li, J. Zhang, W. Chen, Y. Zhang, Exploration of TiO_2 nanoparticle mediated microdynamic therapy on cancer treatment, Nanomedicine 18 (2019) 272–281.
[22] X. Ma, X. Ren, X. Guo, C. Fu, Q. Wu, L. Tan, H. Li, W. Zhang, X. Chen, H. Zhong, Multifunctional iron-based metal−organic framework as biodegradable nanozyme for microwave enhancing dynamic therapy, Biomaterials 214 (2019), 119223.
[23] Q. Wu, N. Xia, D. Long, L. Tan, W. Rao, J. Yu, C. Fu, X. Ren, H. Li, L. Gou, P. Liang, J. Ren, L. Li, X. Meng, Dual-functional supernanoparticles with microwave dynamic therapy and microwave thermal therapy, Nano Lett. 19 (8) (2019) 5277–5286.
[24] T. Tang, X. Xu, Z. Wang, J. Tian, Y. Yang, C. Ou, H. Bao, T. Liu, Cu_2ZnSnS_4 nanocrystals for microwave thermal and microwave dynamic combination tumor therapy, Chem. Commun. 55 (87) (2019) 13148–13151.
[25] C. Fu, H. Zhou, L. Tan, Z. Huang, Q. Wu, X. Ren, J. Ren, X. Meng, Microwave-activated Mn-doped zirconium metal–organic framework nanocubes for highly effective combination of microwave dynamic and thermal therapies against cancer, ACS Nano 12 (3) (2017) 2201–2210.
[26] N.R. Paudel, D. Shvydka, E.I. Parsai, A novel property of gold nanoparticles: free radical generation under microwave irradiation, Med. Phys. 43 (4) (2016) 1598–1602.
[27] W. Xiong, L. Wang, X. Chen, H. Tang, D. Cao, G. Zhang, W. Chen, Pyridinium-substituted tetraphenylethylene salts-based photosensitizers by varying counter anions: highly efficient photodynamic therapy for cancer cell ablation and bacteria inactivation, J. Mater. Chem. B 8 (24) (2020) 5234–5244.
[28] C.O. Kappe, Controlled microwave heating in modern organic synthesis, Angew. Chem. Int. Ed. 43 (46) (2004) 6250–6284.
[29] I. Kraljić, S.E. Mohsni, A new method for the detection of singlet oxygen in aqueous solutions, Photochem. Photobiol. 28 (4-5) (1978) 577–581.
[30] L. Chen, Y. Chen, W. Zhou, J. Li, Y. Zhang, Y. Liu, Mitochondrion-targeting chemiluminescent ternary supramolecular assembly for in situ photodynamic therapy, Chem. Commun. 56 (62) (2020) 8857–8860.
[31] A. Fedyaeva, A. Stepanov, I. Lyubushkina, T. Pobezhimova, E. Rikhvanov, Heat shock induces production of reactive oxygen species and increases inner mitochondrial membrane potential in winter wheat cells, Biochemistry (Mosc.) 79 (11) (2014) 1202–1210.
[32] T. Wu, J. Huang, Y. Yan, Self-assembly of aggregation-induced-emission molecules, Chem. Asian J. 14 (6) (2019) 730–750.
[33] B.S. Li, X. Huang, H. Li, W. Xia, S. Xue, Q. Xia, B.Z. Tang, Solvent and surface/interface effect on the hierarchical assemblies of chiral aggregation-induced emitting molecules, Langmuir 35 (10) (2019) 3805–3813.
[34] X. Zhen, L. Chudal, N.K. Pandey, J. Phan, X. Ran, E. Amandor, X. Huang, O. Johnson, Y. Ran, W. Chen, A powerful combination of copper-cysteamine nanoparticles with potassium iodide for bacterial destruction, Mater. Sci. Eng. C 110 (2020), 110659.
[35] A. Abdal Dayem, M.K. Hossain, S.B. Lee, K. Kim, S.K. Saha, G.-M. Yang, H.Y. Choi, S.-G. Cho, The role of reactive oxygen species (ROS) in the biological activities of metallic nanoparticles, Int. J. Mol. Sci. 18 (1) (2017) 120.
[36] K. Mothilal, J.J. Inbaraj, R. Gandhidasan, R. Murugesan, Photosensitization with anthraquinone derivatives: optical and EPR spin trapping studies of photogeneration of reactive oxygen species, J. Photochem. Photobiol. Chem. 162 (1) (2004) 9–16.
[37] Y. Nosaka, A.Y. Nosaka, Generation and detection of reactive oxygen species in photocatalysis, Chem. Rev. 117 (17) (2017) 11302–11336.
[38] E.A. Mayeda, A.J. Bard, Production of singlet oxygen in electrogenerated radical ion electron transfer reactions, J. Am. Chem. Soc. 95 (19) (1973) 6223–6226.
[39] D. Min, J. Boff, Chemistry and reaction of singlet oxygen in foods, Compr. Rev. Food Sci. Food Saf. 1 (2) (2002) 58–72.
[40] D.R. Kearns, Physical and chemical properties of singlet molecular oxygen, Chem. Rev. 71 (4) (1971) 395–427.
[41] A.U. Khan, Singlet molecular oxygen from superoxide anion and sensitized fluorescence of organic molecules, Science 168 (3930) (1970) 476–477.

[42] G. Afreen, M. Shoeb, S. Upadhyayula, Effectiveness of reactive oxygen species generated from rGO/CdS QD heterostructure for photodegradation and disinfection of pollutants in waste water, Mater. Sci. Eng. C 108 (2020), 110372.
[43] J. Wang, S. Wang, Reactive species in advanced oxidation processes: formation, identification and reaction mechanism, Chem. Eng. J. 401 (2020), 126158.
[44] J.F. Turrens, Mitochondrial formation of reactive oxygen species, J. Physiol. 552 (2) (2003) 335–344.
[45] K. Kouno, C. Ogawa, Y. Shimomura, H. Yano, Y. Ueda, Interaction of imidazole derivatives with electron acceptors. II. Reaction products of imidazole with p-benzoquinone, Chem. Pharm. Bull. 29 (2) (1981) 301–307.
[46] S. Bae, D. Kim, W. Lee, Degradation of diclofenac by pyrite catalyzed Fenton oxidation, Appl. Catal. B Environ. 134 (2013) 93–102.
[47] X. Luo, H. Hu, Z. Pan, F. Pei, H. Qian, K. Miao, S. Guo, W. Wang, G. Feng, Efficient and stable catalysis of hollow Cu_9S_5 nanospheres in the Fenton-like degradation of organic dyes, J. Hazard Mater. 396 (2020), 122735.
[48] R. Gao, X. Mei, D. Yan, R. Liang, M. Wei, Nano-photosensitizer based on layered double hydroxide and isophthalic acid for singlet oxygenation and photodynamic therapy, Nat. Commun. 9 (1) (2018) 1–10.
[49] W. He, Y. Liu, W.G. Wamer, J.-J. Yin, Electron spin resonance spectroscopy for the study of nanomaterial-mediated generation of reactive oxygen species, J. Food Drug Anal. 22 (1) (2014) 49–63.
[50] T. Mosmann, Rapid colorimetric assay for cellular growth and survival: application to proliferation and cytotoxicity assays, J. Immunol. Methods 65 (1–2) (1983) 55–63.
[51] D. Bratosin, L. Mitrofan, C. Palii, J. Estaquier, J. Montreuil, Novel fluorescence assay using calcein-AM for the determination of human erythrocyte viability and aging, Cytometry Part A: The Journal of the International Society for Analytical Cytology 66 (1) (2005) 78–84.
[52] L. Chudal, N.K. Pandey, J. Phan, O. Johnson, L. Lin, H. Yu, Y. Shu, Z. Huang, M. Xing, J.P. Liu, M.-L. Chen, W. Chen, Copper-cysteamine nanoparticles as a heterogeneous Fenton-like catalyst for highly selective cancer treatment, ACS Appl. Bio Mater. 3 (3) (2020) 1804–1814.
[53] X. Quan, Y.B. Zhang, S. Chen, Y.Z. Zhao, F.L. Yang, Generation of hydroxyl radical in aqueous solution by microwave energy using activated carbon as catalyst and its potential in removal of persistent organic substances, J. Mol. Catal. Chem. 263 (1–2) (2007) 216–222.
[54] S. Li, G. Zhang, P. Wang, H. Zheng, Y. Zheng, Microwave-enhanced Mn-Fenton process for the removal of BPA in water, Chem. Eng. J. 294 (2016) 371–379.
[55] N. Wang, T. Zheng, J. Jiang, P. Wang, Cu(II)–Fe(II)–H_2O_2 oxidative removal of 3-nitroaniline in water under microwave irradiation, Chem. Eng. J. 260 (2015) 386–392.
[56] J. Sanz, J. Lombrana, A. De Luis, M. Ortueta, F. Varona, Microwave and Fenton's reagent oxidation of wastewater, Environ. Chem. Lett. 1 (1) (2003) 45–50.
[57] S. Shahin, V.P. Singh, R.K. Shukla, A. Dhawan, R.K. Gangwar, S.P. Singh, C. M. Chaturvedi, 2.45 GHz microwave irradiation-induced oxidative stress affects implantation or pregnancy in mice, Mus musculus, Appl. Biochem. Biotechnol. 169 (5) (2013) 1727–1751.
[58] V.I. Bruskov, L.V. Malakhova, Z.K. Masalimov, A.V. Chernikov, Heat-induced formation of reactive oxygen species and 8-oxoguanine, a biomarker of damage to DNA, Nucleic Acids Res. 30 (6) (2002) 1354–1363.
[59] N. Getoff, Generation of $^1O_2$ by microwave discharge and some characteristic reactions: a short review, Radiat. Phys. Chem. 45 (4) (1995) 609–614.
[60] H. Lin, Y. Shen, D. Chen, L. Lin, B.C. Wilson, B. Li, S. Xie, Feasibility study on quantitative measurements of singlet oxygen generation using singlet oxygen sensor green, J. Fluoresc. 23 (1) (2013) 41–47.
[61] G.N. De Iuliis, R.J. Newey, B.V. King, R.J. Aitken, Mobile phone radiation induces reactive oxygen species production and DNA damage in human spermatozoa in vitro, PloS One 4 (7) (2009) e6446.
[62] Y.-S. Lu, B.-T. Huang, Y.-X. Huang, Reactive oxygen species formation and apoptosis in human peripheral blood mononuclear cell induced by 900 MHz mobile phone radiation, Oxid. Med. Cell. Longev. 2012 (2012), 740280.
[63] J. Friedman, S. Kraus, Y. Hauptman, Y. Schiff, R. Seger, Mechanism of short-term ERK activation by electromagnetic fields at mobile phone frequencies, Biochem. J. 405 (3) (2007) 559–568.
[64] X. Li, N. Kwon, T. Guo, Z. Liu, J. Yoon, Innovative strategies for hypoxic-tumor photodynamic therapy, Angew. Chem. Int. Ed. 57 (2018) 11522–11531.
[65] M. Wu, Z. Liu, W. Zhang, An ultra-stable bio-inspired bacteriochlorin analogue for hypoxia-tolerant photodynamic therapy, Chem. Sci. 12 (2021) 1295–1301.